Received: 22 October 2023 | Revised: 23 March 2024 | Accepted: 21 April 2024

DOI: 10.1002/qj.4748

Quarterly Journal of the Royal Meteorological Society RMetS

RESEARCH ARTICLE

Effects of surface moisture flux on the formation and evolution of cold fog over complex terrain with large-eddy simulation

Xin Li | **Zhaoxia Pu**

Department of Atmospheric Sciences, University of Utah, Salt Lake City, Utah, USA

Correspondence
Zhaoxia Pu, Department of Atmospheric Sciences, University of Utah, 135 S 1460 E, Rm. 819, Salt Lake City, UT 84112, USA.
Email: zhaoxia.pu@utah.edu

Funding information
U. S. National Sceince Foundation, Division of Atmospheric and Geospace Sciences, Grant/Award Number: Award#2049100

Abstract

This study examines the effect of surface moisture flux on fog formation, as it is an essential factor of water vapor distribution that supports fog formation. A one-way nested large-eddy simulation embedded in the mesoscale community Weather Research and Forecasting model is used to examine the effect of surface moisture flux on a cold fog event over the Heber Valley on January 16, 2015. Results indicate that large-eddy simulation successfully reproduces the fog over the mountainous valley, with turbulent mixing of the fog aloft in the valley downward. However, the simulated fog is too dense and has higher humidity, a larger mean surface moisture flux, more extensive liquid water content, and longer duration relative to the observations. The sensitivity of fog simulations to surface moisture flux is then examined. Results indicate that reduction of surface moisture flux leads to fog with a shorter duration and a lower height extension than the original simulation, as the decrease in surface moisture flux impairs water vapor transport from the surface. Consequently, the lower humidity combined with the cold air helps the model reproduce a realistic thin fog close to the observations. The outcomes of this study illustrate that a minor change in moisture flux can have a significant impact on the formation and evolution of fog events over complex terrain, even during the winter when moisture flux is typically very weak.

KEYWORDS

complex terrain, fog, large-eddy simulation, surface moisture flux, WRF

1 | INTRODUCTION

Accurate fog forecasts are desirable owing to the significant impacts of fog events on aviation, other types of transportation, and human health. However, fog prediction remains a challenge with current numerical weather prediction models (Román-Cascón *et al.*, 2019; Steeneveld *et al.*, 2015; Tudor, 2010; Van der Velde *et al.*, 2010; Zhou *et al.*, 2012). Over a mountainous valley's complex terrain, fog prediction is even more challenging, mainly because the mechanism of fog formation is complicated in such areas (Gultepe *et al.*, 2007, 2009, 2016; Müller *et al.*, 2010; Price, 2011; Pu, 2017; Pu *et al.*, 2016; Steeneveld *et al.*, 2015). Previous studies have indicated

that cold fog events forming in small-scale mountainous valleys, such as the Heber Valley in northern Utah in the United States, are particularly difficult to forecast because of complicated interactions among complex terrain, snow on the ground, thermally driven flow, a stable boundary layer, and microphysical processes (e.g., Chachere & Pu, 2019; Gultepe *et al.*, 2016; Hang *et al.*, 2016; Pu *et al.*, 2016; Zhang & Pu, 2019).

During the cold season, when temperatures are below 0°C, ephemeral fog prevails near the surface due to super-cold air. However, as indicated by the Mountain Terrain Atmospheric Modeling and Observations (MATERHORN) program conducted over the Heber Valley from January to February 2015 (Fernando *et al.*, 2015; Gultepe *et al.*, 2016), ephemeral fog is not easily represented by conventional meteorological observations and is hard to forecast. During the MATERHORN program, the Weather Research and Forecasting (WRF) model failed to predict all ephemeral fog over the Heber Valley (Pu *et al.*, 2016) while successfully predicting persistent fog over the Salt Lake Valley, about 70 km west of the Heber Valley. Similar to other studies (e.g., Bergot & Guedalia, 1994; Duynkerke, 1999; Guedalia & Bergot, 1994; Maronga & Bosveld, 2017; Steeneveld & de Bode, 2018; Wei *et al.*, 2013), Zhang and Pu (2019) argue that inaccurate surface conditions, namely snow cover, snow depth, and associated surface albedo, affect the radiation process and thus contribute to the accurate prediction of near-surface meteorological elements over the Heber Valley during ephemeral fog events (Chachere & Pu, 2019; Lin *et al.*, 2017). However, fog remains absent in numerical simulations even when colder air is induced by increased surface albedo (Zhang & Pu, 2019).

In theory, fog formation needs sufficient moisture. Therefore, surface moisture flux (QFX) should be another essential factor for fog simulation. Rémy and Bergot (2009) found that radiation fog is very sensitive to soil moisture conditions. Moisture in the soil alters the heat conduction of soil (Guedalia & Bergot, 1994), which in turn alters the QFX, thereby modifying the surface layer environment (Kim & Yum, 2012). Over the ocean, reduced moisture flux, namely latent heat flux, will lead to weak sea fog (Lee *et al.*, 2021). Over land, the movement of water vapor from the soil to the atmospheric surface layer also contributes to fog formation (Adhikari & Wang, 2020). Therefore, the Heber Valley fog simulation should also account for the surface flux effect. So far, no studies have been dedicated to this area. It is not clear whether the water vapor fluxes over the valley are responsible for the fog formation and evolution. In this study, we examine the influence of surface flux on ephemeral fog formation and evolution over the Heber Valley. We attempt to clarify the impact of the surface flux on the fog simulation over complex terrain.

Typically, large-eddy simulations (LES) produce more accurate fog simulations with more accurate turbulence mixing (Cui *et al.*, 2019; Li & Pu, 2022), thus clarifying the study of the effect of QFX on fog evolution over complex terrain. In this study, an LES embedded in the WRF model from Li and Pu (2022) is used to investigate the effect of QFX on a cold fog case over the Heber Valley on January 16, 2015, during the MATERHORN field program. The contribution of the QFX to the dense fog simulated with LES is discussed. The model and data processing, as well as the simulation results and validation with observations, are described in Section 2. The fog formation mechanism is discussed in Section 3. Section 4 discusses the sensitivity of fog to QFX. A summary and concluding remarks are given in Section 5.

2 | WRF–LES SIMULATION AND VALIDATION

2.1 | Description of simulation and analysis methods

As described in Li and Pu (2022), we use the advanced research version of the WRF model (Skamarock *et al.*, 2019) developed by the US National Center for Atmospheric Research in collaboration with the broader community. Specifically, an LES set-up of the WRF model, namely WRF–LES (Version 4.3), is used in a one-way nested configuration to simulate the cold fog over the Heber Valley on January 16, 2015, during the MATERHORN field program. The five-level nested domains have grid meshes (horizontal resolution) of 201×152 (25 km), 301×301 (5 km), 601×601 (1 km), 501×501 (200 m), and 201×201 (40 m). As shown in Figure 1, domains 1 and 2 cover the North American continent; domain 3 covers the state of Utah; domain 4 covers the Heber Valley (approximately 111°24′W, 40°30′N) and part of Salt Lake City; and domain 5 is located in the Heber Valley and its vicinity.

In this study, the Yonsei University (YSU) planetary boundary layer (PBL) scheme (Hong, 2010; Hong *et al.*, 2006) is used in the outer three domains, and the three-dimensional turbulent kinetic energy (TKE) 1.5 closure scheme is used in the inner two domains, namely the LES domains, with no PBL scheme. Based on the sensitivity studies by Chachere and Pu (2019), which focus on the fog case in the same region (i.e., northern Utah), the fog simulation is not sensitive to the choice of different PBL scheme. Li and Pu (2022) commented that the omission of turbulent eddies in the PBL parametrization results in the failure to reproduce the fog in convection-permitting-scale

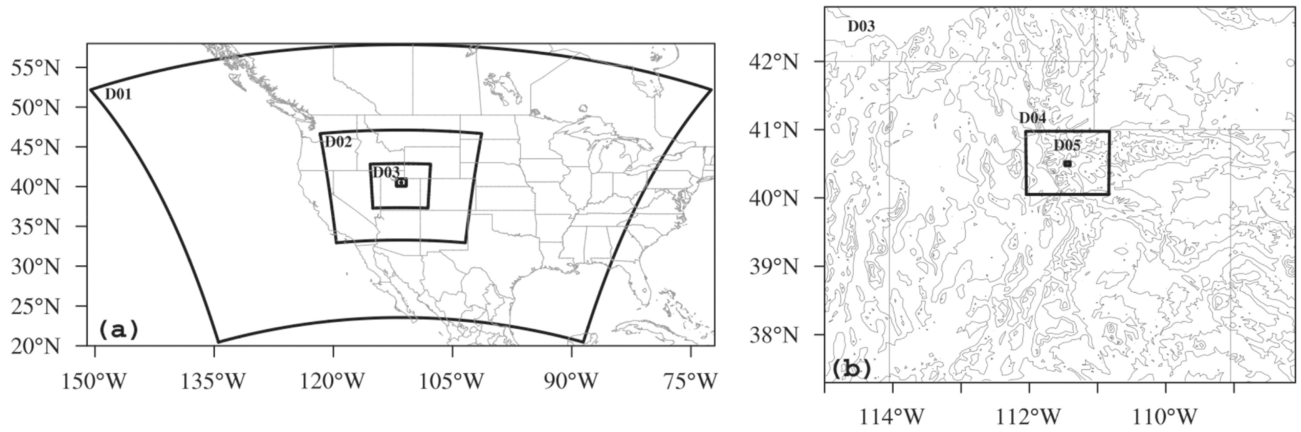

FIGURE 1 (a) Configuration of one-way nested Weather Research and Forecasting–large-eddy simulation domains. (b) Enlarged configuration detail of the inner three domains.

simulation, indicating the LES is necessary for accurate fog simulations. Depending on the horizontal resolution, the Kain and Fritsch (Kain, 2004) deep convection scheme is activated only in domain 1. The Thompson cloud physics scheme (Thompson *et al.*, 2008) for cloud, the Rapid Radiative Transfer Model (Mlawer *et al.*, 1997) for long-wave radiation, the Dudhia scheme (Dudhia, 1989) for short-wave radiation, the Noah land-surface scheme (Chen & Dudhia, 2001) for the land surface, and the revised MM5 Monin–Obukhov scheme for surface parameterizations are used in the simulation.

The National Centers for Environmental Prediction North American Mesoscale Forecast System (NAM) analysis at $12 \times 12\ km^2$ resolution is used to derive the initial and boundary conditions. Sixty-eight vertical levels, of which 33 levels are below 1,500 m, are used in the first four domains. Another well-defined 74 vertical levels, with the lowest model level of ~2 m, are used in domain 5. From the observations, fog occurred on January 16, 2015, from 0735 to 1435 UTC. The numerical simulation was initiated at 0000 UTC on January 15, 2015, and allowed the model a 24-hr spin-up before fog formation.

The YSU PBL scheme directly derives turbulence contributions in the first three domains. In the inner two domains, a horizontal averaging method (5×5 grid average for domain 4 and 25×25 grid average for domain 5) is introduced to the LES results to generate the mean field. Variables such as u, v, w, t, and q are averaged using this method, and the turbulence field with the turbulence signal is then produced by subtracting the mean field from the original LES field (e.g., Li & Pu, 2022). For convenience, in the following discussion we refer to the simulations from the first three domains (domains 1–3) as "WRF simulations" or "WRF" and the simulations from the innermost two domains (domains 4 and 5) as "LES".

2.2 | Simulation results and validation

Fog was observed from 0735 to 1435 UTC on January 16, 2015, over the Heber Valley. By 1200 UTC January 15, northern Utah was under the apex of the ridge at 500 hPa, and the dominant ridging feature was echoed at 250 hPa. At 850 hPa, the surface high-pressure center was present over northern Utah, indicating a favorable synoptic environment for fog to form. Until 0000 UTC January 17, the trough became the dominant feature over northern Utah at 500 hPa, and the fog disappeared at both stations. These synoptic features were well captured by the WRF simulation. This section compares the simulation results from the WRF and LES with the observations to validate the fog simulations over the Heber Valley.

Li and Pu (2022) compared the liquid water content (LWC) at 50 m height from the National Oceanic and Atmospheric Administration's High-Resolution Rapid Refresh (HRRR) analysis products at 3 km horizontal resolution with WRF domains 3 and 4 at 0900 UTC January 16, 2015 (see Li & Pu, 2022, fig. 1). The HRRR analysis is the finest resolution of reliable operational regional analysis available (e.g., Bytheway *et al.*, 2017). The 50 m LWC represents the fog, during which the water vapor becomes saturated and turns into liquid water in the air. In the HRRR analysis, patchy fog covers the Heber Valley from 0800 UTC to 1400 UTC, consistent with observations. The WRF simulation at the convection-permitting scale (1 km horizontal resolution), namely domain 3, fails to reproduce fog over the Heber Valley, similar to previous simulations (Pu *et al.*, 2016; Zhang & Pu, 2019). In contrast, LES in domain 4 successfully reproduces the fog covering almost the entire Heber Valley, with a maximum LWC close to $0.2\ g \cdot kg^{-1}$. However, this simulated fog is much denser than in HRRR, which shows patchy fog covering part of the valley, with a maximum LWC of only $0.02\ g \cdot kg^{-1}$.

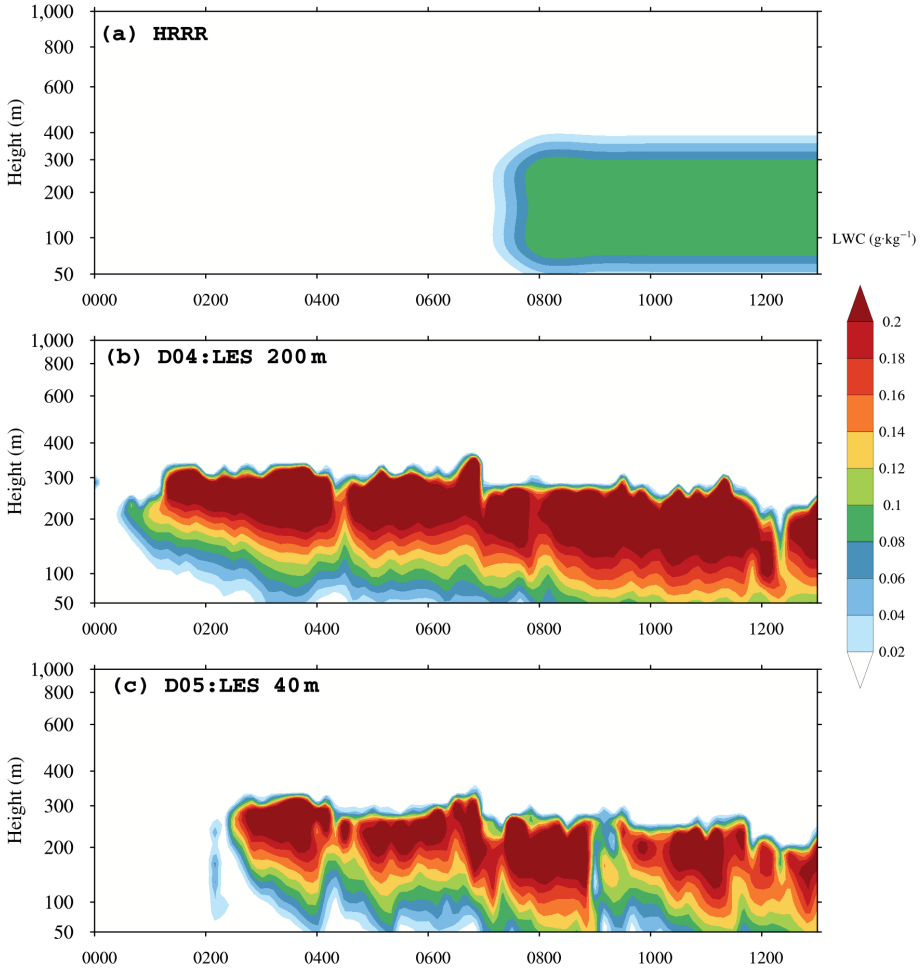

FIGURE 2 Evolution of simulated liquid water content profiles from (a) High-Resolution Rapid Refresh (HRRR) analysis and simulations of (b) domain 4 and (c) domain 5 over the Heber Valley from 0000 to 1300 UTC January 16, 2015. LES: large-eddy simulation. [Colour figure can be viewed at wileyonlinelibrary.com]

Figure 2 compares the evolution of LWC at the MATERHORN field site (located at 111°24′W, 40°30′N) in the Heber Valley from the HRRR (Figure 2a), domain 4 (Figure 2b), and domain 5 (Figure 2c) from 0000 to 1200 UTC January 16, 2015. Consistent with the observed fog event, the fog from HRRR forms at ~0730 UTC and occurs around a height of 50–400 m, with a maximum LWC of over 0.08 g·kg^{-1}. In the LES, both domains 4 and 5 produce dense fog with a maximum LWC of over 0.2 g·kg^{-1}. At the same time, the fog aloft starts in the LES at about 0100 UTC January 16, 2015, nearly right after sunset over the Heber Valley when the air is saturated above 100 m height. Then fog arrives near the ground around 0330 UTC and appears on and off between 0330 UTC and 0730 UTC before becoming a persistent and dense fog between 0730 UTC until past 1200 UTC. In the WRF at 1 km grid spacing in domain 3 (figure not shown), the air is always unsaturated and fog does not form over the Heber Valley.

Figure 3 shows the simulated profiles of wind speed (Figure 3a), air temperature (Figure 3b), relative humidity (RH; Figure 3c), and specific humidity q (Figure 3d) against the sounding data at the Heber Valley field site at 0715 UTC January 16, 2015, before fog formation. Compared with the wind speed in domains 1 and 2, the simulation from domains 3–5 shows a similar low wind, mostly less than 0.5 m·s^{-1}, which agrees with the observations. Since the grid spacing is reduced in domains 3–5, the better wind speed simulation is related to the smaller grid spacing (higher resolution) in the model. For air temperature, LES domains 4 and 5 significantly reduce the air temperature to approximately −6°C at a height of 0–250 m, close to the temperature of −9 to −6°C in observations, whereas the WRF simulation in domains 1–3 overestimates the temperature, with nearly 0–3°C below a height of 500 m. The different air temperatures in the WRF and LES lead to different fog simulations. The warmer air in the WRF here and in previous studies (Pu *et al.*, 2016; Zhang & Pu, 2019) inhibits fog formation, whereas the lower temperature in the LES favors fog formation in the simulation. Meanwhile, the RH in LES is around 100%, corresponding to the simulated fog, and significantly higher than the observation when no fog is formed at the field site. Although WRF does not produce the same fog as the observation at 0715 UTC, the RH from WRF is too low to form fog when the fog occurs at the field site. The q in the LES is also more extensive than that in the WRF simulation and observation. The high-humidity air in the LES combined with the lower temperature makes the air

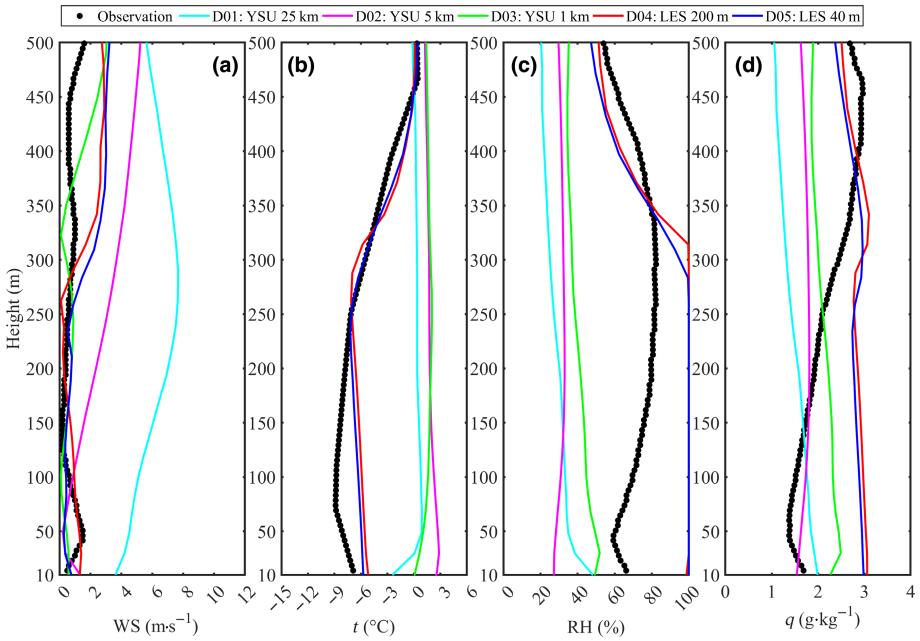

FIGURE 3 Vertical profiles of (a) wind speed (WS), (b) air temperature T, (c) relative humidity (RH), and (d) specific humidity q from simulations against the sounding data over the Heber Valley at 0715 UTC 16 January 2015. YSU: Yonsei University; LES: large-eddy simulation. [Colour figure can be viewed at wileyonlinelibrary.com]

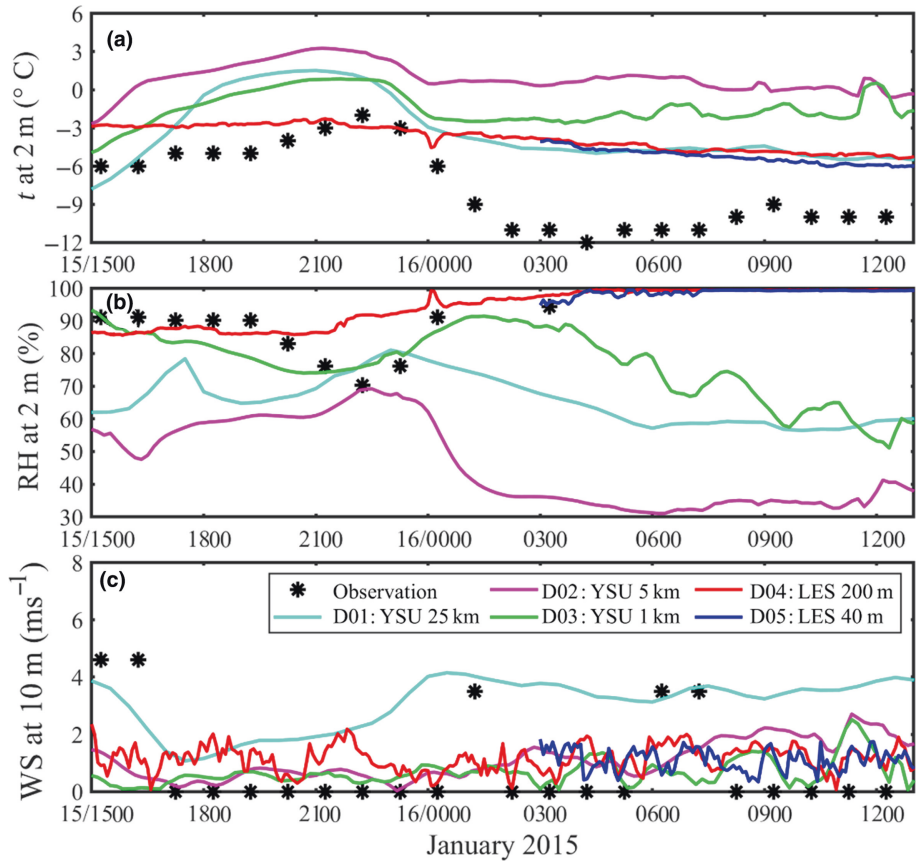

FIGURE 4 Time series of (a) 2-m air temperature, (b) 2-m relative humidity (RH), and (c) 10-m wind speed from simulations against surface Mesonet observations over the Heber Valley from 1500 UTC January 15 to 1300 UTC January 16, 2015. The figure is expanded from Li and Pu (2022) with a longer period of data. [Colour figure can be viewed at wileyonlinelibrary.com]

saturated at the lower level and eventually forms a dense fog. Similar to Figure 3, Li and Pu (2022, fig. 2) showed variable profiles from the simulation and observation at 1115 UTC on January 16, 2015, during the fog event.

Similar to the results at 0715 UTC, domains 3–5 produce a better wind speed simulation than domains 1–2 do at 1115 UTC. LES domains 4–5 again provide the best air temperature simulation, with a temperature lower than −6°C below 250 m altitude. The low temperature in LES is close to the observation, whereas the WRF-simulated air temperature is usually over 0°C, which is significantly higher than the observed value. The air in the LES is kept

saturated with RH of 100%, which is close to the observed RH of 90%.

Gultepe *et al.* (2015) stated that cold fog can form at temperatures below −10°C when RH exceeds 80%. The RH of 100% indicates fog formation in the LES. The WRF-simulated RH is often lower than 50%, and no fog is formed. This implies that the WRF simulation produces warmer and drier air that cannot reproduce the fog over the Heber Valley. Similar to the q at 0715 UTC, the LES also provides a higher value than the observation and WRF simulation. In the LES, the air is not as cold as the observation, but with more moisture and eventual saturation of much of the water vapor a dense fog is generated. Therefore, the dense fog in the LES is related mainly to the more extensive q rather than the cold air temperature over the Heber Valley during the simulation.

Expanded from Li and Pu (2022), Figure 4 shows the time series of 2-m air temperature (Figure 4a), 2-m relative humidity (Figure 4b), and 10-m wind speed (Figure 4c) from the simulations against surface Mesonet observations at the field site in the Heber Valley from 1500 UTC January 15 to 1300 UTC January 16, 2015. Overall, compared with the WRF simulations, the LES provides weak surface winds, colder temperatures, and moister surface air, all of which are closer to the observations.

3 | MECHANISM OF FOG FORMATION

3.1 | Effects of advection

The process of fog formation is complicated over complex terrain (Müller *et al.*, 2010). The convergence of cold flow (Cuxart & Jiménez, 2012; Müller *et al.*, 2010) and gravity waves (Hang *et al.*, 2016) in valleys can influence fog formation there. Li and Pu (2022) verified the critical effect of the horizontal advection of LWC on fog formation over the Heber Valley with WRF–LES simulations. Following Li and Pu (2022), Figure 5 shows the time series of a west–east cross-section of LWC, horizontal flow vectors, and temperature in the Heber Valley at 2300 UTC January 15, and 0000, 0100, 0800, 1000, and 1200 UTC January 16, 2015. After sunset at around 2300 UTC January 15, mountain surface cooling creates saturated supercooled water vapor (fog) near the east side of the mountains at a terrain height

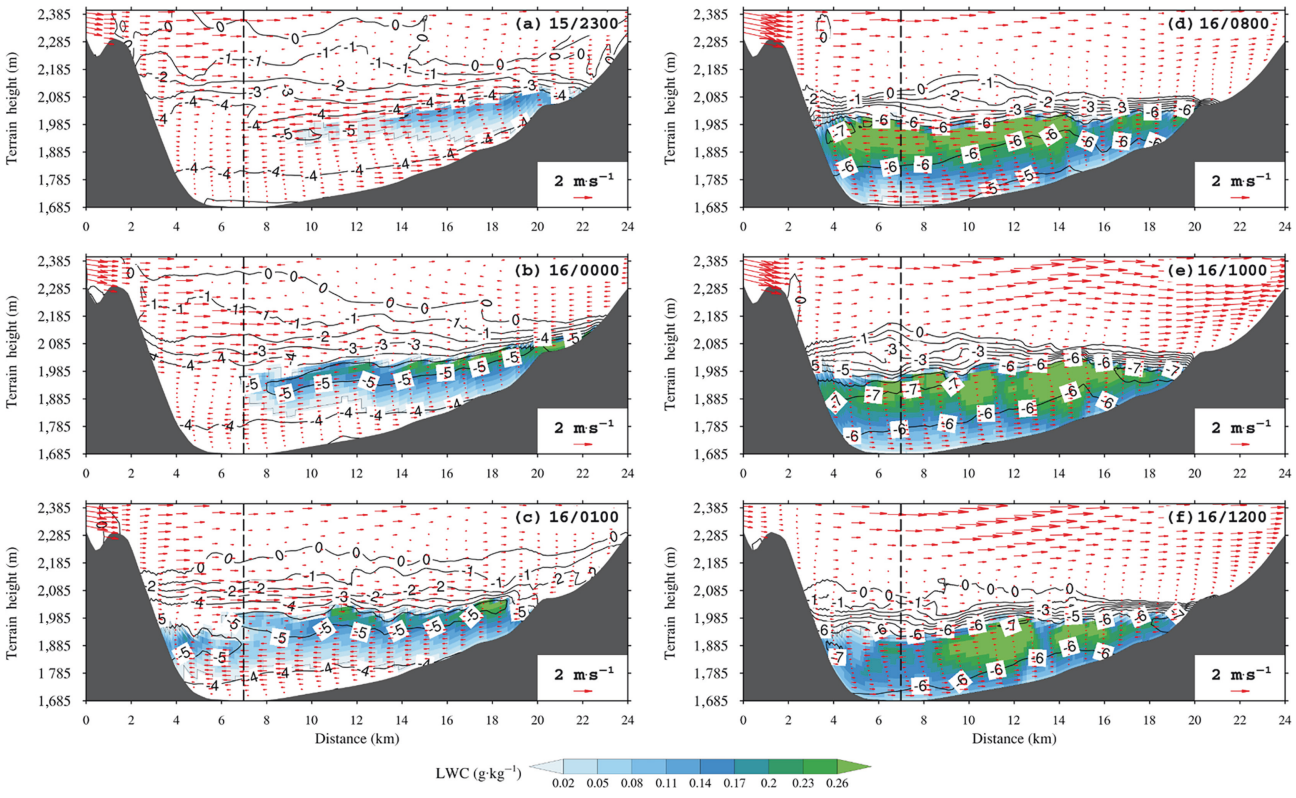

FIGURE 5 West–east cross-section (through the mountainous valley, namely, the black line in Figure 2g–i of Li and Pu 2022) of the simulated liquid water content (LWC; shaded color contours), horizontal flow (vectors), and temperature (contour interval 2°C) before fog formation at (a) 2300 UTC January 15, (b) 0000 UTC January 16, and (c) 0100 UTC January 16, 2015, and during and after fog formation at (d) 0800, (e) 1000, and (f) 1200 UTC January 16, 2015. Mountainous terrain is shaded black. The field site is marked by the black dashed line. The figure is expanded from Li and Pu (2022) with more details. [Colour figure can be viewed at wileyonlinelibrary.com]

of ~2,000 m (Figure 5a), which is then transported aloft over the valley by horizontal winds (Figure 5a–c). The easterly winds induce the spread of saturated water vapor, reflecting the significant impact of horizontal advection on fog formation over the Heber Valley (Li & Pu, 2022). Once the fog moves aloft over the valley, the fog is gradually transported down to the ground (Figure 5d–f).

Meanwhile, after 0100 UTC January 16, corresponding to radiative cooling at the fog top during the evening and night, the near-surface air temperature decreases. At 0800 UTC January 16, the saturated ultra-cold (below −5°C) water vapor spreads over the valley floor, indicating fog formation in the Heber Valley (Figure 5d). At 1000 and 1200 UTC January 16, the near-surface air temperature continues to decrease, dropping to −6°C, enhancing water vapor saturation and leading to dense fog over the Heber Valley (Figure 5e,f).

3.2 | Turbulent mixing

Considering the importance of PBL processes during fog events (e.g., Roach *et al.*, 1976; Román-Cascón *et al.*, 2012; Welch & Wielicki, 1986; Ye *et al.*, 2015; Westerhuis *et al.*, 2020), more accurate vertical mixing effects in the LES generally lead to better simulations of meteorological elements (Cui *et al.*, 2019; Li & Pu, 2022; Mazoyer *et al.*, 2017). Specifically, over the Heber Valley, strong wind shear can generate a strong turbulent mixing effect. Figure 6a shows the evolution of TKE with height in domain 5 at the field site from 0000 to 1300 UTC January 16, 2015. Compared with the near-zero value of TKE in the WRF simulation, the strong turbulence is reproduced in the LES, with a TKE maximum of over 5 $m^2 \cdot s^{-2}$. Figure 6b shows the variation of the LWC tendency from the contribution of advection, turbulent mixing, and microphysics from 0000 to 0800 UTC January 15. The stronger eddies in the LES help the vertical mixing of the LWC and dominate LWC variation in the Heber Valley. Zhou and Ferrier (2008) suggested that there is a balance of turbulence intensity for fog formation, either to maintain or destroy. In this study, the dense fog was accompanied with strong turbulence mixing, indicating the strong turbulence did not exceed the intensity threshold. Once the horizontal advection spreads the saturated water vapor over the whole valley aloft, the moderate turbulent eddies (against to the threshold) mix the LWC vertically and finally form fog at the valley floor. In the WRF simulation, the air is stable and only surface cooling through long-wave radiation and surface flux can reduce the air temperature. The weak vertical mixing in the WRF causes warmer air over the Heber Valley to suppress fog formation.

3.3 | Mechanism of dense fog formation

Because of the strong turbulence, the LES generates colder air over the Heber Valley. However, the cold air explains only the fog formation, not the larger LWC (relative to observations) in the LES, especially with the air not as cold as the observations (e.g., Figure 3b). In reality, the larger moisture in LES enhances fog formation and causes dense fog. Therefore, it is necessary to investigate the

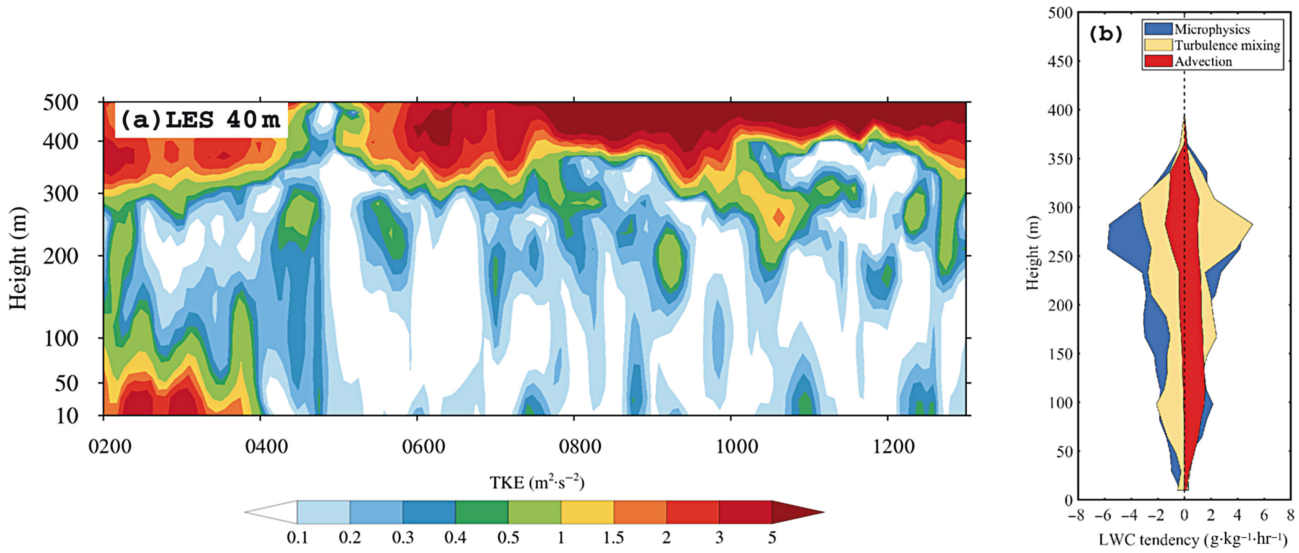

FIGURE 6 (a) Evolution of turbulent kinetic energy (TKE) profiles from simulation of domain 5 over the Heber Valley from 0200 to 1300 UTC January 16, 2015. LES: large-eddy simulation. (b) Variation of the liquid water content (LWC) tendency from the contribution of advection, turbulent mixing, and microphysics over the Heber Valley before fog formation from 0200 to 0800 UTC January 16, 2015 based on domain 5. [Colour figure can be viewed at wileyonlinelibrary.com]

mechanism leading to the higher humidity in the air. Since atmospheric conditions are usually sensible to surface conditions (Kim & Yum, 2012; Lee *et al.*, 2021), the higher humidity in the LES may be associated with stronger moisture support from the surface. This section analyzes surface fluxes in the WRF and LES to examine their influence on air humidity.

3.3.1 | Radiation flux

Figure 7 shows the upward long-wave radiation (Figure 7a), downward long-wave radiation (Figure 7b), sensible heat flux (Figure 7c), and latent heat flux (Figure 7d) from the WRF and LES against surface Mesonet observations at the Heber Valley field site from 1500 UTC January 15 to 1300 UTC January 16, 2015. During the day, LES are closer to observations for both upward and downward long-wave radiation. At night, the dense fog leads to large downward long-wave radiation in the LES, increasing surface temperature and upward long-wave radiation on the surface. Although the LES generates a latent heat flux closer to the observation, the LES flux is nearly twice as large as the observations during the day (20 vs. 10 $W \cdot m^{-2}$). Lee *et al.* (2021) stated that reduced moisture flux results in weak fog, implying that high moisture flux is associated with dense fog. Therefore, the higher moisture in the air during dense fog is potentially related to the larger latent heat flux, namely the moisture flux, in the LES.

3.3.2 | Surface moisture flux

QFX can affect air moisture during a fog period (Kim & Yum, 2012; Lee *et al.*, 2021). In this section, the QFX simulated by WRF is compared with that simulated by LES to explore the effect of QFX during dense fog. Since domains 4 and 5 provide similar QFX in the Heber Valley, and domain 4 covers a larger area that contains environmental QFX (QFX at the mountaintops and out of the valley) that is important for dense fog at the field site, the following comparison will use results from domain 4 for the LES. Figure 8 shows the mean QFX from domain 3 (Figure 8a), domain 4 (Figure 8b), and the mean QFX difference between domains 3 and 4 and the mean 10-m wind in domain 4 (Figure 8c) during the simulation period from 0000 UTC January 15 to 1300 UTC January 16, 2015. The figures indicate that domain 3 generates a mean QFX of less than 18 $g \cdot m^{-2} \cdot hr^{-1}$, while domain 4 produces a larger QFX, especially at the mountaintops and over the valley. The QFX increments in LES can be as high as over 10 $g \cdot m^{-2} \cdot hr^{-1}$ at the mountaintops and 4 $g \cdot m^{-2} \cdot hr^{-1}$ over the Heber Valley. The larger mean QFX implies larger water vapor support from the land surface in the LES. Combined with the convergent flow over the valley shown in Figure 8c, the water vapor accumulates and forms a dense fog.

In the land surface and surface parameterization scheme, QFX is computed from the surface exchange coefficient of moisture C_q and the difference in q between the land surface and the lowest model level:

$$\mathrm{QFX} = \kappa \rho C_q (q_s - q_a) U, \tag{1}$$

where ρ is the density of water, U is wind speed at 10-m height, κ is the von Kármán constant, equal to 0.4, q_s is the specific humidity at the land surface calculated from the land surface temperature t_s, and q_a is the specific humidity at the lowest model level computed from the air temperature at the lowest model level t_a.

Despite the similar wind speed from the WRF and the LES, the key factors C_q, q_s, and q_a in Equation (1)

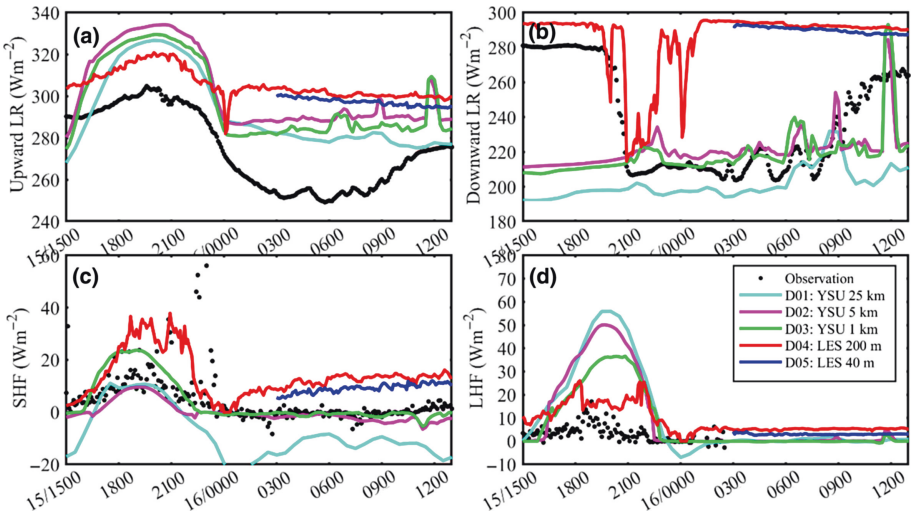

FIGURE 7 Time series of surface (a) upward long-wave radiation (LR), (b) downward long-wave radiation, (c) sensible heat flux (SHF), and (d) latent heat flux (LHF) from simulations against surface Mesonet observations over the Heber Valley from 1500 UTC January 15 to 1300 UTC January 16, 2015. [Colour figure can be viewed at wileyonlinelibrary.com]

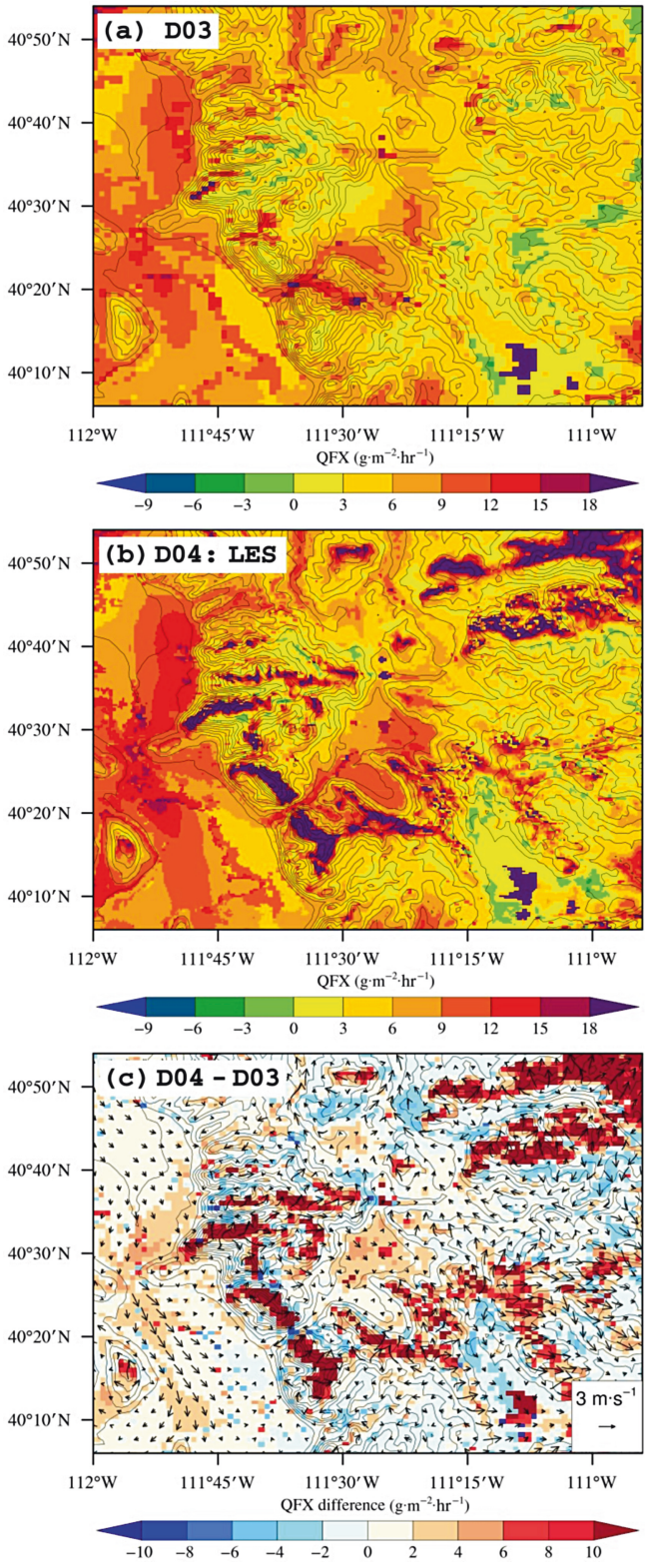

FIGURE 8 Mean surface moisture flux (QFX, shaded contour) from simulations of (a) domain 3 and (b) domain 4 from 0000 UTC January 15 to 1300 UTC January 16, 2015. (c) Mean difference in QFX between simulations of domains 3 and 4 from 0000 UTC January 15 to 1300 UTC January 16, 2015. Terrain height is added as line contours. Mean 10-m wind from simulation of domain 4 is added in (c). [Colour figure can be viewed at wileyonlinelibrary.com]

for QFX are distinguished in Figure 9. Figure 9 shows the time series of QFX (Figure 9a), C_q (Figure 9b), and q at the land surface (q_s) and the lowest model level (q_a; Figure 9c) at the field site in domains 3 and 4 from 0000 UTC January 15 to 1300 UTC January 16, 2015. After 0400 UTC January 15, the QFX in domain 4 gradually becomes larger than that in domain 3. Only at noon is QFX weaker than in domain 3. Similarly, C_q in domain 4 is also larger than that in domain 3 after 0400 UTC January 15, except at noon. The q_s in domain 3 (around 2 g·kg^{-1}) is greater than q_a (around 3 g·kg^{-1}) during the daytime (before 1500 UTC January 15 and after 0000 UTC January 16). This negative q difference between the soil and atmosphere ($q_s - q_a$) in domain 3 results in a negative QFX, although C_q is constantly changing. However, the q_s in domain 4 is around 4 g·kg^{-1}, which is significantly larger than the q_s in domain 3 after 0400 UTC January 15, except at noon. The q_a in domain 4 is only slightly larger than that in domain 3. Therefore, the large q_s (except at noon) in domain 4 leads to a large positive difference between q_s and q_a, which combines with the large C_q to generate a large QFX in domain 4. Since $q_s - q_a$ is mostly positive in domain 4, QFX in domain 4 is larger than that in domain 3.

To further investigate the QFX impact and the reason why $q_s - q_a$ is often positive in the LES, Figure 10 shows the time series of accumulated q (ACQ) from QFX (Figure 10a), land surface temperature t_s and lowest model level air temperature t_a (Figure 10b), and downward long-wave radiation (Figure 10c) in domains 3 and 4 at the field site from 0000 UTC January 15 to 1300 UTC January 16, 2015. Owing to the larger QFX in the LES, the ACQ from domain 4 (over 280 g·m^{-2}) is significantly larger than that from domain 3 (~110 g·m^{-2}). The larger ACQ in the LES indicates stronger evaporation of water vapor from the soil to the air and explains the larger q_a in domain 4, which is related to dense fog. Like the humidity, t_s in domain 3 is usually less than t_a at night. The t_s in domain 4 is greater than t_a after 0400 UTC January 15, similar to the evolution of q_s. The increased t_s in domain 4 is associated with the extremely increased downward long-wave radiation. After fog formation, the downward radiation increases (shown in Figure 7b). In the parametrization scheme, q_s is usually computed according to t_s, since land surface RH is equal to 100% in the model. Intense downward long-wave radiation (around 300 W·m^{-2}) weakens the surface cooling at night and helps maintain the surface temperature t_s, and consequently increases q_s in the LES. Finally, a larger q_s leads to a larger QFX in domain 4. In domain 3, the downward long-wave radiation is usually weak, around 210 W·m^{-2}. The surface cooling effect dominates t_s, making t_s and q_s lower and resulting in weak QFX. The difference in QFX

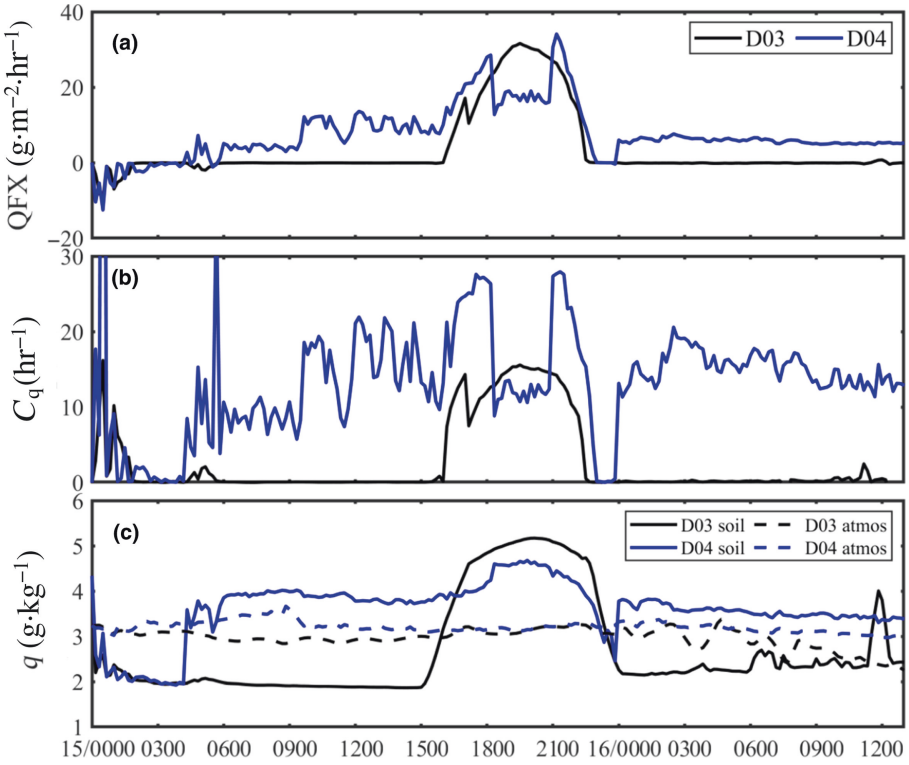

FIGURE 9 Time series of (a) surface moisture flux (QFX), (b) surface exchange coefficient of moisture (C_q), and (c) specific humidity (q) at the land surface and the lowest model level from simulations of domains 3 and 4 over the Heber Valley from 0000 UTC January 15 to 1300 UTC January 16, 2015. [Colour figure can be viewed at wileyonlinelibrary.com]

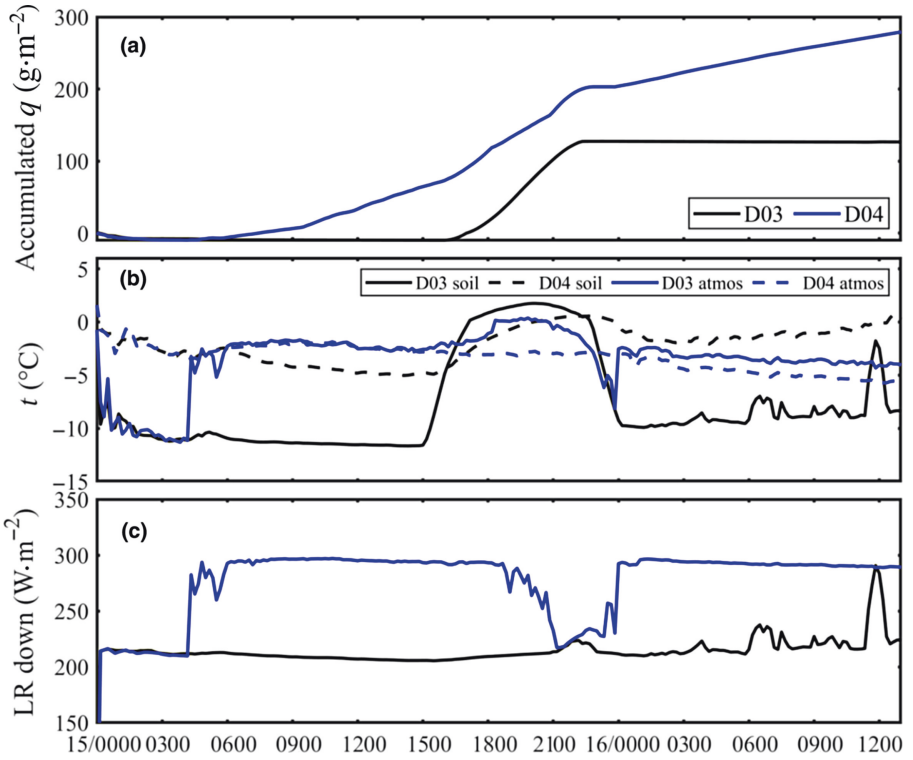

FIGURE 10 Time series of (a) accumulated specific humidity (q) from surface moisture flux (QFX), (b) temperature at the land surface and the lowest model level, and (c) downward long-wave radiation (LR) from simulations of domains 3 and 4 over the Heber Valley from 0000 UTC January 15 to 1300 UTC January 16, 2015. [Colour figure can be viewed at wileyonlinelibrary.com]

between domains 3 and 4 leads to different water vapor contents in these two domains. The larger water vapor content in domain 4 contributes to the simulated dense fog over the Heber Valley during the observation project.

4 | SENSITIVITY OF FOG SIMULATIONS TO QFX

The aforementioned analysis reveals a potential link between larger QFX and large specific humidity during

dense fog in the LES over the Heber Valley. To further clarify the relationship between QFX and dense fog in the LES, this section describes a series of sensitivity experiments. In the experiments, positive QFX during the LES is respectively reduced 0.5 (0.5QFX), 0.3 (0.3QFX), and 0.1 times (0.1QFX).

Figure 11 compares the time series of QFX (Figure 11a) and ACQ from QFX (Figure 11b) in domains 3 and 4 at the Heber Valley field site from 0000 UTC January 15 to 1300 UTC January 16, 2015. The simulated QFX and ACQ gradually decrease with decreasing QFX by the multiplying coefficients (0.5–0.1). At 1300 UTC January 16, ACQ from 0.5QFX is very close to that in domain 3, with a value of about 120 $g \cdot m^{-2}$.

Figure 12 compares the evolution of LWC at the Heber Valley field site from 0.5QFX (Figure 12a), 0.3QFX (Figure 12b), and 0.1QFX (Figure 12c) from 0000 to 1200 UTC January 16, 2015. Compared with the original LES results in Figure 2b,c, all the sensitivity experiments show weakening fog. The height of the fog gradually moves downward from the original LES of 300 m to 0.5QFX of 200 m, 0.3QFX of 100 m, and 0.1QFX of 50 m. Fog formation is also delayed from the original LES at 0100 UTC to 0.5QFX at 0500 UTC, to 0.3QFX at 0700 UTC, and to 0.1QFX at 1000 UTC January 16, 2015. Similar to Lee *et al.* (2021), who studied the QFX impact on ocean fog, the weakened fog with reduced QFX indicates the significant impact of QFX on the fog simulation over the Heber Valley. The colder air, caused by the intense turbulence and convergence of cold flow, combined with the larger specific humidity, which is induced by the QFX from the surface, forms a dense fog in the LES. Once QFX is reduced, the dense fog can be weakened and is closer to the observation.

Figure 13 shows the profiles of wind speed (Figure 13a), air temperature (Figure 13b), RH (Figure 13c), and q (Figure 13d) from the sensitivity studies against sounding data at the Heber Valley field site at 1115 UTC January 16, 2015, during the fog period. The figures indicate that the wind speed from all sensitivity experiments is low and close to the observations. From the temperature profile, the simulated inversion layer gradually moves downward with reduced QFX. The low-level air temperature gradually decreases from −6°C to −9°C with reduced QFX. Meanwhile, in the sensitivity experiments, the height of the inversion layer is also reduced. The q at the low level decreases from 3 $g \cdot kg^{-1}$ to 2.3 $g \cdot kg^{-1}$ with reduced QFX. The decrease in q in the sensitivity experiments implies a critical influence of QFX on the evolution of q in the LES. A large QFX results in larger q in the LES, which enhances the fog, until dense fog finally forms over the Heber Valley. As QFX decreases, surface cooling at the mountaintops is weakened with the convergence of cold flows over the Heber Valley. Local surface cooling and turbulence dominate the air temperature over the Heber Valley. Therefore,

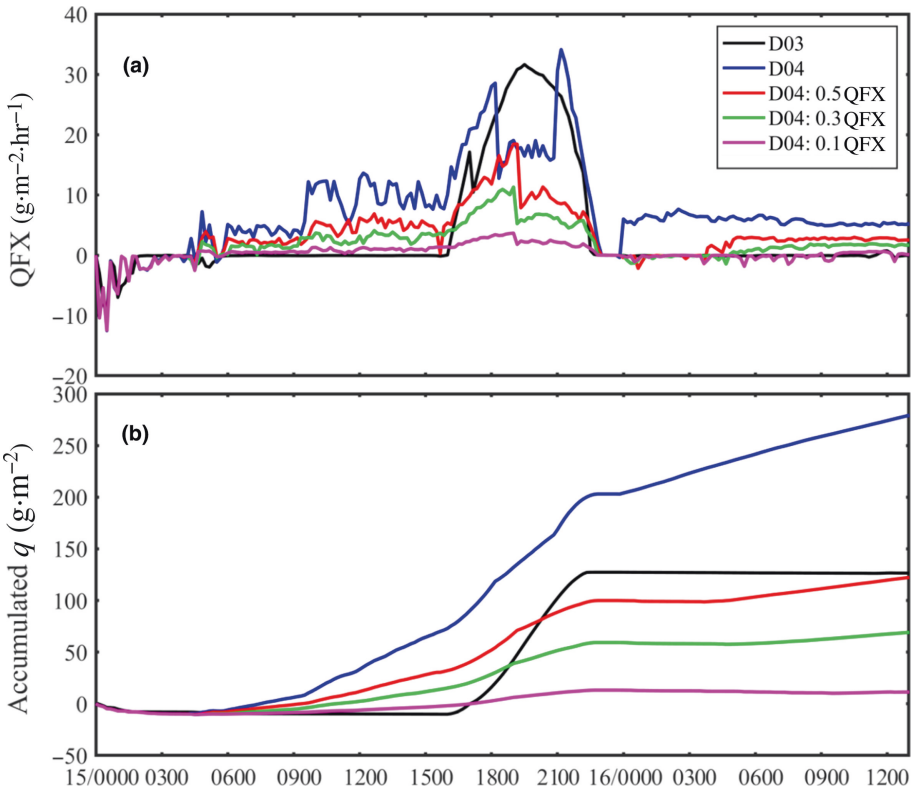

FIGURE 11 Time series of (a) surface moisture flux (QFX) and (b) accumulated specific humidity (q) from QFX from simulations of domains 3 and 4, and sensitivity studies over the Heber Valley from 0000 UTC January 15 to 1300 UTC January 16, 2015. [Colour figure can be viewed at wileyonlinelibrary.com]

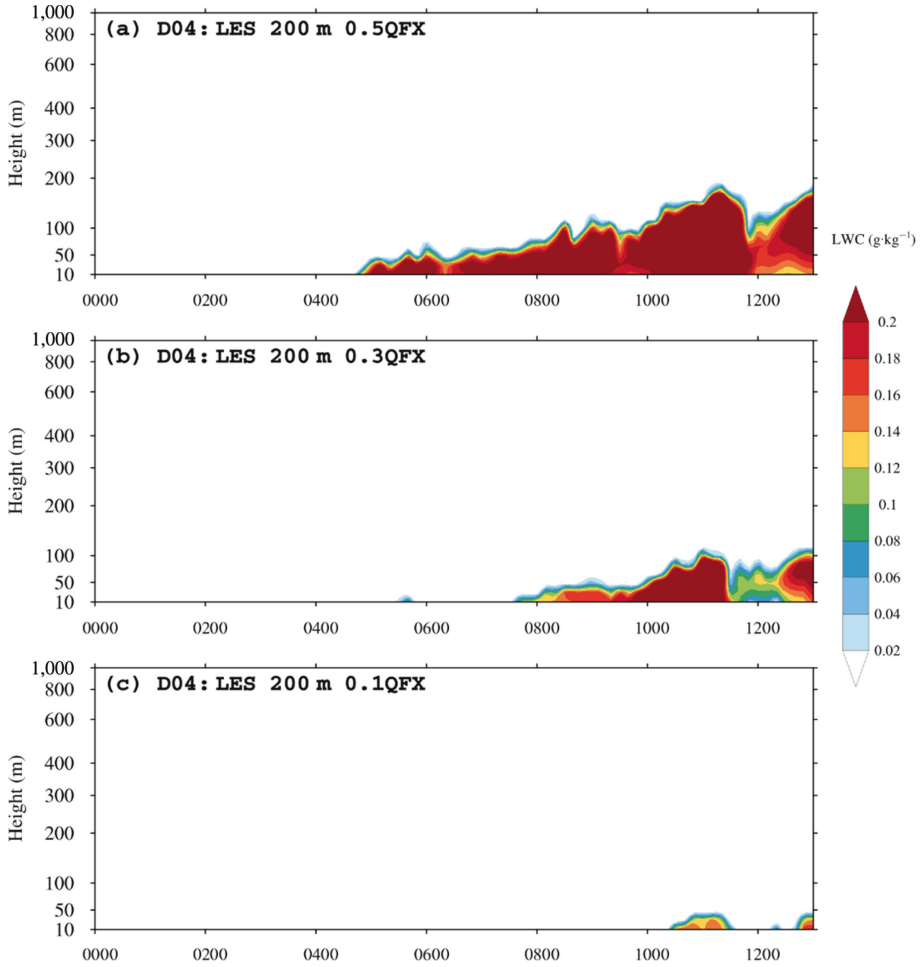

FIGURE 12 Evolution of liquid water content profiles from sensitivity experiments with (a) 0.5QFX, (b) 0.3QFX, and (c) 0.1QFX over the Heber Valley from 0000 to 1300 UTC 16 January 2015. LES: large-eddy simulation; QFX: surface moisture flux. [Colour figure can be viewed at wileyonlinelibrary.com]

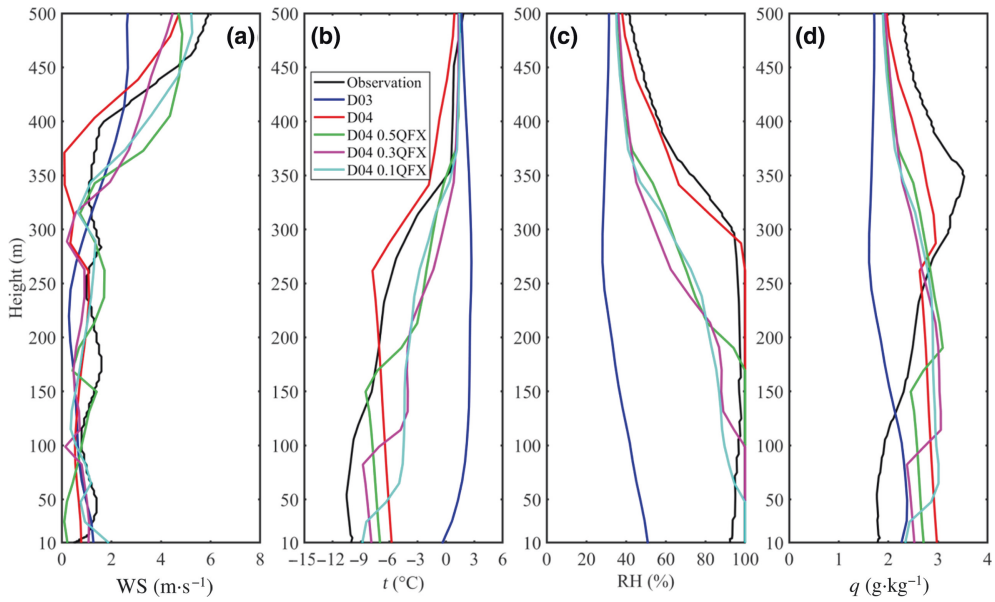

FIGURE 13 Vertical profiles of (a) wind speed (WS), (b) air temperature (t), (c) relative humidity (RH), and (d) specific humidity (q) from simulations and sensitivity experiments against the sounding data over the Heber Valley at 1115 UTC January 16, 2015. QFX: surface moisture flux. [Colour figure can be viewed at wileyonlinelibrary.com]

the inversion layer becomes thinner in the sensitivity experiments.

Nevertheless, the modification of QFX may not be realistic in actual cases. Since there are multiple physical and dynamic processes associated with fog, the sensitivity experiments do not reproduce a perfect vertical profile of the meteorological elements against the observations. The initial condition from NAM analysis data may also

have uncertainties that could lead to the failure on LWC simulations for the fog event over the Heber Valley. Meanwhile, the HRRR data, rather than the observation of LWC (which is not observed during the field experiment), is used for validation, making the accurate fog simulation and validation more challenging. Nevertheless, the sensitivity results here imply the critical effect of QFX during the fog simulation. A small change in moisture flux can have a significant impact on the formation and evolution of fog events over complex terrain. During the LES, the precise turbulent mixing simulation makes the fog simulation more sensible to surface flux.

5 | SUMMARY AND CONCLUSION

In this study, a one-way nested WRF–LES model is used to explore the impact of QFX on a cold fog event over complex terrain in the Heber Valley in northern Utah in the United States during the MATERHORN fog program on January 16, 2015. During the fog event, the near-surface air temperature dropped to −12°C at night and was conducive to cold fog formation. Previous WRF simulations (Pu *et al.*, 2016; Zhang & Pu, 2019) and WRF simulations at the cloud-permitting scale (~1 km) in this study do not capture the near-surface temperature and humidity and thus fail to reproduce the fog, whereas the LES successfully reproduces the fog over the valley with strong turbulence. The strong turbulent eddies vertically mix the fog aloft in the valley, which is transported by horizontal advection, forming fog on the valley floor. However, the air humidity in the LES is too high and forms a too-dense fog with more extensive LWC and a longer duration.

Compared with the WRF simulation, the LES provides larger QFX (namely, latent heat flux) over the mountaintops and the small valley. During the simulation period, the larger QFX doubles the moisture support to the atmosphere over the Heber Valley. The connection of moisture flux, air humidity, and dense fog indicates the relationship between moisture flux and the dense fog in the LES over the Heber Valley. The sensitivity experiments indicate that the overestimated water vapor flux is responsible for the dense fog in the LES. The reduction in moisture flux weakens water vapor transport from the surface. Lower humidity combined with cold air forms a thin fog closer to the field observations. Therefore, accurate specification of QFX over complex terrain is critical for numerical simulations of fog formation and evolution. This is especially important for LES, which provide more accurate turbulence simulations and make fog formation more sensitive to surface conditions (Smith *et al.*, 2021). Even though moisture flux is usually very weak during the winter, a slight change in moisture flux will result in significantly different fog over complex terrain. This study highlights the importance of surface flux observations for better understanding and prediction of cold fog over complex terrain. A recent field program, Cold Fog Amongst Complex Terrain (Pu *et al.*, 2023), made comprehensive observations in the same study areas. Future work will emphasize extended studies with Cold Fog Amongst Complex Terrain cases and observations.

ACKNOWLEDGEMENTS

This study is supported by U. S. National Sceince Foundation, Division of Atmospheric and Geospace Sciences Award #2049100 (Cold Fog Amongst ComplTerrain). The computational resources and support from the UCAR CISL supercomputing system and the Center for High-Performance Computing (CHPC) at the University of Utah are appreciated. The National Centers for Environmental Prediction NAM data are obtained from the National Center for Atmospheric Research's Research Data Archive (https://rda.ucar.edu/datasets/ds609.0/).

DATA AVAILABILITY STATEMENT

Data available on request from the authors.

ORCID

Zhaoxia Pu https://orcid.org/0000-0003-4461-1789

REFERENCES

Adhikari, B. & Wang, L. (2020) The potential contribution of soil moisture to fog formation in the Namib Desert. *Journal of Hydrology*, 591, 125326.

Bergot, T. & Guedalia, D. (1994) Numerical forecasting of radiation fog. Part I: numerical model and sensitivity tests. *Monthly Weather Review*, 122(6), 1218–1230. Available from: https://doi.org/10.1175/1520-0493(1994)122%3C1218:NFORFP%3E2.0.CO;2

Bytheway, J.L., Kummerow, C.D. & Alexander, C. (2017) A features-based assessment of the evolution of warm season precipitation forecasts from the HRRR model over three years of development. *Weather and Forecasting*, 32, 1841–1856. Available from: https://doi.org/10.1175/WAF-D-17-0050.1

Chachere, C.N. & Pu, Z. (2019) Numerical simulations of an inversion fog event in the salt lake valley during the MATERHORN-fog field campaign. *Pure and Applied Geophysics*, 176(5), 2139–2164. Available from: https://doi.org/10.1007/s00024-018-1770-8

Chen, F. & Dudhia, J. (2001) Coupling an advanced land surface–hydrology model with the Penn State–NCAR MM5 modeling system. Part I: model implementation and sensitivity. *Monthly Weather Review*, 129(4), 569–585. Available from: https://doi.org/10.1175/1520-0493(2001)129<0569:CAALSH>2.0.CO;2

Cui, C., Bao, Y., Yuan, C., Li, Z. & Zong, C. (2019) Comparison of the performances between the WRF and WRF-LES models in radiation fog–a case study. *Atmospheric Research*, 226, 76–86. Available from: https://doi.org/10.1016/j.atmosres.2019.04.003

Cuxart, J. & Jiménez, M.A. (2012) Deep radiation fog in a wide closed valley: study by numerical modeling and remote sensing. *Pure and Applied Geophysics*, 169(5), 911–926. Available from: https://doi.org/10.1007/s00024-011-0365-4

Dudhia, J. (1989) Numerical study of convection observed during the winter monsoon experiment using a mesoscale two-dimensional model. *Journal of Atmospheric Sciences*, 46(20), 3077–3107. Available from: https://doi.org/10.1175/1520-0469(1989)046<3077:NSOCOD>2.0.CO;2

Duynkerke, P.G. (1999) Turbulence, radiation and fog in Dutch stable boundary layers. *Boundary-Layer Meteorology*, 90(3), 447–477. Available from: https://doi.org/10.1023/A:1026441904734

Fernando, H.J.S., Pardyjak, E.R., Di Sabatino, S., Chow, F.K., De Wekker, S.F.J., Hoch, S.W. et al. (2015) The MATERHORN: unraveling the intricacies of mountain weather. *Bulletin of the American Meteorological Society*, 96(11), 1945–1967. Available from: https://doi.org/10.1175/BAMS-D-13-00131.1

Guedalia, D. & Bergot, T. (1994) Numerical forecasting of radiation fog. Part II: a comparison of model simulation with several observed fog events. *Monthly Weather Review*, 122(6), 1231–1246. Available from: https://doi.org/10.1175/1520-0493(1994)122<1231:NFORFP>2.0.CO;2

Gultepe, I., Fernando, H.J.S., Pardyjak, E.R., Hoch, S.W., Silver, Z., Creegan, E. et al. (2016) An overview of the MATERHORN fog project: observations and predictability. *Pure and Applied Geophysics*, 173(9), 2983–3010. Available from: https://doi.org/10.1007/s00024-016-1374-0

Gultepe, I., Pearson, G., Milbrandt, J.A., Hansen, B., Platnick, S., Taylor, P. et al. (2009) The fog remote sensing and modeling field project. *Bulletin of the American Meteorological Society*, 90(3), 341–360. Available from: https://doi.org/10.1175/2008BAMS2354.1

Gultepe, I., Tardif, R., Michaelides, S.C., Cermak, J., Bott, A., Bendix, J. et al. (2007) Fog research: a review of past achievements and future perspectives. *Pure and Applied Geophysics*, 164(6), 1121–1159. Available from: https://doi.org/10.1007/s00024-007-0211-x

Gultepe, I., Zhou, B., Milbrandt, J., Bott, A., Li, Y., Heymsfield, A.J. et al. (2015) A review on ice fog measurements and modeling. *Atmospheric Research*, 151, 2–19. Available from: https://doi.org/10.1016/j.atmosres.2014.04.014

Hang, C., Nadeau, D.F., Gultepe, I., Hoch, S.W., Román-Cascón, C., Pryor, K. et al. (2016) A case study of the mechanisms modulating the evolution of valley fog. *Pure and Applied Geophysics*, 173(9), 3011–3030. Available from: https://doi.org/10.1007/s00024-016-1370-4

Hong, S.Y. (2010) A new stable boundary-layer mixing scheme and its impact on the simulated east Asian summer monsoon. *Quarterly Journal of the Royal Meteorological Society*, 136(651), 1481–1496. Available from: https://doi.org/10.1002/qj.665

Hong, S.Y., Noh, Y. & Dudhia, J. (2006) A new vertical diffusion package with an explicit treatment of entrainment processes. *Monthly Weather Review*, 134(9), 2318–2341. Available from: https://doi.org/10.1175/MWR3199.1

Kain, J.S. (2004) The Kain–Fritsch convective parameterization: an update. *Journal of Applied Meteorology*, 43(1), 170–181. Available from: https://doi.org/10.1175/1520-0450(2004)043<0170:TKCPAU>2.0.CO;2

Kim, C.K. & Yum, S.S. (2012) A numerical study of sea-fog formation over cold sea surface using a one-dimensional turbulence model coupled with the weather research and forecasting model. *Boundary-Layer Meteorology*, 143(3), 481–505.

Lee, E., Kim, J.H., Heo, K.Y. & Cho, Y.K. (2021) Advection fog over the eastern Yellow Sea: WRF simulation and its verification by satellite and in situ observations. *Remote Sensing*, 13(8), 1480. Available from: https://doi.org/10.3390/rs13081480

Li, X. & Pu, Z. (2022) Turbulence effects on the formation of cold fog over complex terrain with large-eddy simulation. *Geophysical Research Letters*, 49, e2022GL098792. Available from: https://doi.org/10.1029/2022GL098792

Lin, C., Zhang, Z., Pu, Z. & Wang, F. (2017) Numerical simulations of an advection fog event over Shanghai Pudong international airport with the WRF model. *Journal of Meteorological Research*, 31(5), 874–889. Available from: https://doi.org/10.1007/s13351-017-6187-2

Maronga, B. & Bosveld, F.C. (2017) Key parameters for the life cycle of nocturnal radiation fog: a comprehensive large-eddy simulation study. *Quarterly Journal of the Royal Meteorological Society*, 143(707), 2463–2480. Available from: https://doi.org/10.1002/qj.3100

Mazoyer, M., Lac, C., Thouron, O., Bergot, T., Masson, V. & Musson-Genon, L. (2017) Large eddy simulation of radiation fog: impact of dynamics on the fog life cycle. *Atmospheric Chemistry and Physics*, 17(21), 13017–13035. Available from: https://doi.org/10.5194/acp-17-13017-2017

Mlawer, E.J., Taubman, S.J., Brown, P.D., Iacono, M.J. & Clough, S.A. (1997) Radiative transfer for inhomogeneous atmospheres: RRTM, a validated correlated-k model for the longwave. *Journal of Geophysical Research: Atmospheres*, 102(D14), 16663–16682. Available from: https://doi.org/10.1029/97JD00237

Müller, M.D., Masbou, M. & Bott, A. (2010) Three-dimensional fog forecasting in complex terrain. *Quarterly Journal of the Royal Meteorological Society*, 136(653), 2189–2202. Available from: https://doi.org/10.1002/qj.705

Price, J. (2011) Radiation fog. Part I: observations of stability and drop size distributions. *Boundary-Layer Meteorology*, 139(2), 167–191. Available from: https://doi.org/10.1007/s10546-010-9580-2

Pu, Z. (2017) Surface data assimilation and near-surface weather prediction over complex terrain. In: Park, S.K. & Xu, L. (Eds.) *Data assimilation for atmospheric Oceanic and hydrologic applications*, Vol. III. Switzerland: Springer, pp. 219–240. Available from: https://doi.org/10.1007/978-3-319-43415-5&uscore;10

Pu, Z., Chachere, C.N., Hoch, S.W., Pardyjak, E. & Gultepe, I. (2016) Numerical prediction of cold season fog events over complex terrain: the performance of the WRF model during MATERHORN-fog and early evaluation. *Pure and Applied Geophysics*, 173(9), 3165–3186. Available from: https://doi.org/10.1007/s00024-016-1375-z

Pu, Z., Pardyjak, E., Hoch, S., Gultepe, I., Hallar, A.G., Perelet, A. et al. (2023) Cold fog amongst complex terrain. *Bulletin of the American Meteorological Society* https://journals.ametsoc.org/view/journals/bams/aop/BAMS-D-22-0030.1/BAMS-D-22-0030.1.xml, 104, E2030–E2052.

Rémy, S. & Bergot, T. (2009) Assessing the impact of observations on a local numerical fog prediction system. *Quarterly Journal of the Royal Meteorological Society*, 135(642), 1248–1265.

Roach, W.T., Brown, R., Caughey, S.J., Garland, J.A. & Readings, C.J. (1976) The physics of radiation fog: I–a field study. *Quarterly Journal of the Royal Meteorological Society*, 102(432), 313–333. Available from: https://doi.org/10.1002/qj.49710243204

Román-Cascón, C., Yagüe, C., Sastre, M., Maqueda, G., Salamanca, F. & Viana, S. (2012) Observations and WRF simulations of fog events at the Spanish Northern Plateau. *Advances in Science and Research*, 8(1), 11–18. Available from: https://doi.org/10.5194/asr-8-11-2012

Román-Cascón, C., Yagüe, C., Steeneveld, G.J., Morales, G., Arrillaga, J.A., Sastre, M. et al. (2019) Radiation and cloud-base lowering fog events: observational analysis and evaluation of WRF and HARMONIE. *Atmospheric Research*, 229, 190–207. Available from: https://doi.org/10.1016/j.atmosres.2019.06.018

Skamarock, W.C., Klemp, J.B., Dudhia, J., Gill, D.O., Liu, Z., Berner, J. et al. (2019) A description of the advanced Research WRF ModelVersion 4. NCAR Tech. Note NCAR/TN-5561STR. pp. 145.

Smith, D.K., Renfrew, I.A., Dorling, S.R., Price, J.D. & Boutle, I.A. (2021) Sub-km scale numerical weather prediction model simulations of radiation fog. *Quarterly Journal of the Royal Meteorological Society*, 147(735), 746–763. Available from: https://doi.org/10.1002/qj.3943

Steeneveld, G.J. & de Bode, M. (2018) Unravelling the relative roles of physical processes in modelling the life cycle of a warm radiation fog. *Quarterly Journal of the Royal Meteorological Society*, 144(714), 1539–1554. Available from: https://doi.org/10.1002/qj.3300

Steeneveld, G.J., Ronda, R.J. & Holtslag, A.A.M. (2015) The challenge of forecasting the onset and development of radiation fog using mesoscale atmospheric models. *Boundary-Layer Meteorology*, 154(2), 265–289. Available from: https://doi.org/10.1007/s10546-014-9973-8

Thompson, G., Field, P.R., Rasmussen, R.M. & Hall, W.D. (2008) Explicit forecasts of winter precipitation using an improved bulk microphysics scheme. Part II: implementation of a new snow parameterization. *Monthly Weather Review*, 136(12), 5095–5115. Available from: https://doi.org/10.1175/2008MWR2387.1

Tudor, M. (2010) Impact of horizontal diffusion, radiation and cloudiness parameterization schemes on fog forecasting in valleys. *Meteorology and Atmospheric Physics*, 108(1), 57–70. Available from: https://doi.org/10.1007/s00703-010-0084-x

Van der Velde, I.R., Steeneveld, G.J., Schreur, B.W. & Holtslag, A.A.M. (2010) Modeling and forecasting the onset and duration of severe radiation fog under frost conditions. *Monthly Weather Review*, 138(11), 4237–4253. Available from: https://doi.org/10.1175/2010MWR3427.1

Wei, L., Pu, Z. & Wang, S. (2013) Numerical simulation of the life cycle of a persistent wintertime inversion over Salt Lake City. *Boundary Layer Meteorology*, 148(2), 399–418. Available from: https://doi.org/10.1007/s10546-013-9821-2

Welch, R.M. & Wielicki, B.A. (1986) The stratocumulus nature of fog. *Journal of Applied Meteorology and Climatology*, 25(2), 101–111. Available from: https://doi.org/10.1175/1520-0450(1986)025<0101:TSNOF>2.0.CO;2

Westerhuis, S., Fuhrer, O., Cermak, J. & Eugster, W. (2020) Identifying the key challenges for fog and low stratus forecasting in complex terrain. *Quarterly Journal of the Royal Meteorological Society*, 146(732), 3347–3367. Available from: https://doi.org/10.1002/qj.3849

Ye, X., Wu, B. & Zhang, H. (2015) The turbulent structure and transport in fog layers observed over the Tianjin area. *Atmospheric Research*, 153, 217–234. Available from: https://doi.org/10.1016/j.atmosres.2014.08.003

Zhang, F. & Pu, Z. (2019) Sensitivity of numerical simulations of near-surface atmospheric conditions to snow depth and surface albedo during an ice fog event over Heber Valley. *Journal of Applied Meteorology and Climatology*, 58(4), 797–811. Available from: https://doi.org/10.1175/JAMC-D-18-0064.1

Zhou, B., Du, J., Gultepe, I. & Dimego, G. (2012) Forecast of low visibility and fog from NCEP: current status and efforts. *Pure and Applied Geophysics*, 169(5), 895–909. Available from: https://doi.org/10.1007/s00024-011-0327-x

Zhou, B. & Ferrier, B.S. (2008) Asymptotic analysis of equilibrium in radiation fog. *Journal of Applied Meteorology and Climatology*, 47, 1704–1722. Available from: https://doi.org/10.1175/2007JAMC1685.1

How to cite this article: Li, X. & Pu, Z. (2024) Effects of surface moisture flux on the formation and evolution of cold fog over complex terrain with large-eddy simulation. *Quarterly Journal of the Royal Meteorological Society*, 1–15. Available from: https://doi.org/10.1002/qj.4748